Kent Academic Repository

Peters, Jonathan J. P., Bristowe, Nicholas C., Rusu, Dorin, Apachitei, Geanina, Beanland, Richard, Alexe, Marin and Sanchez, Ana M. (2020) *Polarisation screening mechanisms at La0.7Sr0.3MnO3-PbTiO3 interfaces.* ACS Applied Materials & Interfaces, 12 (9). pp. 10657-10663. ISSN 1944-8244.

Polarisation screening mechanisms at La$_{0.7}$Sr$_{0.3}$MnO$_3$-PbTiO$_3$ interfaces

Jonathan J. P. Peters*[1], Nicholas C. Bristowe[2], Dorin Rusu[1], Geanina Apachitei[1], Richard Beanland[1], Marin Alexe[1], Ana M. Sanchez[1]

[1] Department of Physics, University of Warwick, Coventry, United Kingdom

[2] School of Physical Sciences, University of Kent, Canterbury, United Kingdom

*corresponding author: j.peters.1@warwick.ac.uk

Abstract

The structural, electronic and magnetic properties of interfaces between epitaxial La$_{0.7}$Sr$_{0.3}$MnO$_3$ and PbTiO$_3$ have been explored via atomic resolution transmission electron microscopy of a functional multiferroic tunnel junction. Measurements of the polar displacements and octahedral tilting show the competition between the two distortions at the interface, and demonstrate a strong dependence on the polarisation orientation. Density functional theory provides information on the electronic and magnetic properties, where the interface termination plays a crucial role in the screening mechanisms.

Introduction

Polarisation screening at metal-ferroelectric interfaces has been a puzzling issue since the dawn of ferroelectric thin films. This screening from free charge in the metal is crucial in ferroelectric films for reducing the depolarising field created by the separation of the bound charges. This depolarising field acts to reduce the polarisation with the extreme case of completely annihilating it.[1] Early studies suggested that the polarisation should decrease at the ferroelectric-metal interfaces vanishing either within the ferroelectric[2,3] or by penetrating the electrodes for a finite range, usually related to the Thomas-Fermi screening length.[4] In all scenarios the thin films suffered high depolarising fields that would, in the extreme case of ultra-thin films, totally suppress the ferroelectric polarisation. Improved growth techniques for ferroelectric thin films now allow these predictions to be tested by the experimental realisation of such ultrathin films. Interestingly, ferroelectricity has been found to exist in films only a few unit cells in thickness (e.g. in PbTiO$_3$,[5,6] BaTiO$_3$,[7] and BiFeO$_3$[8]), suggesting sufficient screening can be achieved. This has allowed the development of structures with novel properties through the manipulation of their order parameters (e.g. polarisation, strain, magnetism).[5,6,9,10] Within these structures, interface effects still play a crucial role. By altering the electronic and mechanical boundaries,[5,11–13] new functional properties such as conduction and magnetism can emerge.[14–17] This has empowered the development of novel ferroelectric based nanoelectronic devices. Many parameters at the interface (such as strain, conductivity and composition) can influence the observed polarisation,[5,18] which are often competing and provide a complex array of options to engineer desired properties. As

perovskite thin film devices are made ever smaller, interface effects, and their control, become ever more important.

The ferroelectric tunnel junction (FTJ) is a promising ferroelectric device that uses a ferroelectric as a dielectric tunnel barrier in an asymmetric capacitor structure.[18,19] The asymmetric electrodes provide different charge screening, which controls the barrier height due to the bound charges at the interfaces when the polarisation is switched. This in turn is used to modulate a tunnelling current across the ferroelectric, giving tunnelling electroresistance (TER). One reason this device has gained attention is its ability to be combined with ferromagnetic electrodes, combining the TER and tunnelling magnetoresistance (TMR) effects to form a 4-state multiferroic tunnel junction (MFTJ).[18] A popular MFTJ construction is $La_{0.7}Sr_{0.3}MnO_3$ (LSMO) and $PbTiO_3$ (PTO) layers epitaxially grown on a $SrTiO_3$ (STO) substrate followed by a sputtered Co layer. PTO is a common ferroelectric used due to its ability to sustain large polarisation and ease of growth whilst LSMO is used as bottom electrode since its pseudocubic perovskite structure is a close lattice match to the STO and PTO. Additionally, LSMO is a highly ferromagnetic mixed-valence manganite with a Curie temperature around 370 K and a large magnetoresistance.[18,20,21] Combined with the ferromagnetic top Co electrode, a functional MFTJ is formed.

First-principles studies have demonstrated that the screening effects at the PTO-Co interface consist of spin and polarisation dependent charge transfer between d-orbitals of the Co and Ti at the interface.[22,23] On the other hand, the bottom PTO-LSMO interface is quite different, and the focus of most theoretical studies has been on what happens to the LSMO at the interfaces. It has been reported that the ionic displacement of the cations that produce the polarization in the ferroelectric might continue into the oxide electrode, i.e. the oxide electrode can share the ionic displacements of the ferroelectric layer. The ionic displacements in the electrode help decrease the local dipole at the interface which is created from the imperfect screening of the free charges.[11] Furthermore, the underlying lattice of LSMO has a charged-plane structure, with an alternating net charge in each (001) layer of $+0.7\ e^-$ and $-0.7\ e^-$ per 2D formula unit. Therefore, the LSMO termination will have an effective net bound charge that either screens or reinforces the ferroelectric polarisation.[24,25] However, additional effects can arise from structural deformations and distortions in the crystals. Note that whilst the LSMO/PTO lattice mismatch is low, LSMO and PTO have quite dissimilar crystal structures. PTO has a tetragonal $P4mm$ structure, with cooperative off centring of the Ti and O ions. Conversely, LSMO has a non-polar $R\bar{3}c$ structure containing an $a^-a^-a^-$ ($a^-a^-c^-$ under biaxial strain) octahedral tilting pattern (using Glazer notation).[26]

Interfaces between such contrasting structures have been known to give rise to novel electronic and magnetic properties, as well as structural changes.[25,27–30] In general, it may be expected that polarisation will penetrate into the electrodes, preventing a large discontinuity in the bound charge that cannot otherwise be screened effectively by the imperfect metals. However, it is well known that polar displacements are often antithetical to "antiferrodistortive" octahedral tilting.[31] At the LSMO-PTO interface, there is competition between charge screening, lattice strain and sub-unit cell structural conflicts that must be reconciled. The LSMO-PTO (or other ferroelectrics) system has attracted great interest, both theoretically and experimentally, since it constitutes an

interfacial multiferroic. Initial theoretical studies by Burton et al (2009)[32], and later Bristowe et al (2012)[33], showed that the reversal of the polarization in a ferroelectric film, such as $BaTiO_3$ (BTO), leads to a change in the magnetic properties in La-manganite materials, predicting a substantial interfacial magnetoelectric effect. More crucially, it is possible to use the polarisation to cause a magnetic phase transition (from ferromagnetic to antiferromagnetic) that is normally induced via composition changes. Hammouri et al. (2016)[34] also reported that the properties of the LSMO in the LSMO-$PbZr_{0.2}Ti_{0.8}O_3$ (PZT) system behaved differently depending on the PZT polarization. If PZT polarization pointed towards the LSMO/PZT interface a magnetization enhancement was observed, whereas if the polarization was away from the interface an opposite effect of the magnetization, i.e. reduction, occurred in the system. Additionally, it has been demonstrated experimentally by Preziosi et al. (2015)[35] that the ferroelectric polarization of PZT is capable to modulate the interfacial magnetism of the $L_{0.825}Sr_{0.175}MnO_3$. Yu et al. (2019)[36] showed similar effects for PZT-LSMO but also noted the effects of strain in modifying the LSMO's bond lengths and therefore magnetic properties. Nevertheless, although it was not mentioned directly, the theoretical results shown by Burton and Hammouri revealed that structural changes occur not only in a few LSMO monolayers but also in the first monolayer of the ferroelectric materials, (BTO and PZT).

This article constitutes an extensive analysis of the LSMO/PTO interface, and the screening mechanisms, at atomic level. The extreme dimensions of the devices, and more so the interfaces, make aberration corrected scanning transmission electron microscopy (STEM) imaging an essential tool to examine the structure. Using STEM, a detailed characterization of displacements and distortions, including octahedral tilting, with picometre resolution has been performed. Thus, the competition between two structural parameters, the oxygen octahedral tilting in LSMO and the polar ionic displacement in PTO has been explored. These experimental measurements are combined with DFT calculations, shedding light onto the multiferroic interface in the STO/LSMO/PTO/Co functional MFTJ. This is linked back to the measured TER/TMR properties, and could provide a path to optimising or engineering future heterostructures.

Methodology

Samples where grown using reflection high energy electron diffraction assisted pulsed laser deposition using a 248 nm wavelength KrF excimer laser. Atomically smooth vicinal surfaces were prepared on (100)-oriented STO substrates (nominal 0.1° miscut) by chemical etching in $H_2O:NH_4F:HY$ solution (100:3:1 concentration) and thermal annealing at 950 °C for 2 h. For the bottom electrode, 60 unit cells of $(La_{0.7}Sr_{0.3})MnO_3$ (LSMO) was deposited at 600 C using 0.9 mJ cm^2 laser fluence at 0.2 Hz repetition rate in 0.15 mbar O_2 atmosphere. The PTO ferroelectric barrier was then deposited at 600 °C, 0.2 mbar O_2 pressure, 0.45 mJ cm_2 laser fluence and 4 Hz repetition rate. The top contact Co was finally deposited by RF sputtering at 2.5×10^3 mbar Ar pressure and 20 W applied power. Finally, 40×40 μm^2 electrodes were patterned into the Co using photolithography and wet-etching of the Co film.

Atomic resolution STEM images were acquired using a double aberration corrected JEOL ARM-200F operating at 200 kV. Annular dark field (ADF) images were formed using a collection angle of 45-180 mrad and annular

bright field (ABF) images were formed using collection angles of 11-23 mrad.[37] TEM specimens were prepared using a JEOL 4500-JIB using standard lift-out procedures. Atomic coordinates were measured by finding local pixel maxima which were then refined using least squares fitting, taking into account nearest neighbour peak contributions.

Electrical characterisation was performed on 40×40 μm^2 devices using a Keithley 2635 source-measure unit and an HTTP4 Lake-Shore cryogenic probing station. Total magnetic moment was measured on the total area (5×5 mm^2) using an Oxford Instruments MagLab vibrating sample magnetometer. Measurements were performed in the as grown state after cooling to 10 K under a -0.8 T field. TMR is calculated as $\frac{R_{\uparrow\downarrow} - R_{\uparrow\uparrow}}{R_{\uparrow\uparrow}}$ where $R_{\uparrow\uparrow}$ and $R_{\uparrow\downarrow}$ are the resistances of the device with parallel and antiparallel magnetisations of the electrodes.

Density-Functional-Theory (DFT) calculations were performed using the spin polarized Wu-Cohen (WC) exchange correlation functional,[38] as implemented in the Siesta code.[39,40] The La/Sr doping was treated using the virtual crystal approximation (VCA) and full details of the pseudopotentials and numerical atomic orbitals are given in Refs. [41,42]. WC, in combination with these pseudopotentials and numerical atomic orbitals, was previously found appropriate to describe both ferromagnetic and ferroelectric properties of similar multiferroic interfaces.[33] The DFT calculations focussed on the LSMO-PTO interface and consisted of a slab geometry of between 11.5-12 unit cells of LSMO, 6-6.5 unit cells of PTO, and a 2.1 nm thick vacuum layer. The thickness of each layer was found sufficient to observe bulk-like features in the centre of each. The in plane lattice parameter was constrained to match STO, with a $\sqrt{2} \times \sqrt{2}$ periodicity to allow for octahedral tilting. A 3x3x1 Monkhorst-Pack grid and a 700 Ry cut-off for real space integrations were found necessary to accurately capture the octahedral tilting and polar distortions.[40] A dipole correction was employed to enforce zero macroscopic field in the vacuum layer. Finite-D calculations were run by adapting the PTO surface oxygen chemistry with either fluorine or nitrogen through the VCA. This allowed us to simulate the effect of imperfect screening of these ultrathin films, and also allowed us to avoid entering the pathological regime whereby the metal fermi level enters the ferroelectric conduction band due to the DFT band gap error.[33,43] While both La,SrO-TiO_2 and MnO_2-PbO interfaces were simulated, the La,SrO-TiO_2 calculations with $D \geq 0$ were found to enter the pathological regime and so were not studied any further. This is unfortunate as the experimental samples were found to consist of this termination, however comparison between the $D < 0$ La,SrO-TiO_2 and MnO_2-PbO interfaces can be made (see supporting information).

Results & discussion

To investigate the polarisation and octahedral tilting, standard ADF STEM imaging based on the collection of high-angle scattered electrons is insufficient. Whilst useful for its atomic number contrast, this is a double-edged sword that also means it is not able to resolve lighter elements such as oxygen. This absence of information from the oxygen atoms is obviously an issue for measuring octahedral tilt, but it also reduces the accuracy of any polarisation measurements. To mitigate these issues, ABF imaging is chosen as a suitable technique to be able to resolve all the atomic positions. ABF images are formed taking mainly electrons that have been scattered

at low angles. It is similar to standard bright field imaging but excluding electrons scattered close to the optic axis. This technique is less sensitive to atomic number and therefore allows the imaging of all atoms in the LSMO-PTO structure. An additional issue that must be taken into account in order to resolve all atomic positions arises from the fact that STEM images correspond to a projection of the structure. Figures 1(a) and 1(b) shows the projection of the PTO structure along $\langle 100 \rangle$ and $\langle 110 \rangle$ directions respectively. Only the latter projection has no overlap between titanium and oxygen, allowing the titanium displacement with respect to the centre of the oxygen octahedron, Δ_B, to be measured. The polarization in the PTO is proportional to, and in the same direction as, Δ_B. As mentioned above, octahedral tilts are present in the LSMO crystal structure. A consequence of the antiphase tilt system in LSMO is that the oxygen octahedral tilts are not visible along a pseudocubic $\langle 100 \rangle$ direction as the tilt averages to zero (see Fig. 1(c)). To reveal the structure of the LSMO a $\langle 110 \rangle$ direction must be used, as shown in Fig. 1(d). However, only three of the six distinct pseudocubic $\langle 110 \rangle$ projections are suitable to reveal and measure the oxygen octahedral tilting. The measured tilt angle, θ_{110}, can be easily converted to the Glazer notation (i.e. the tilt about the $\langle 100 \rangle$ directions) using simple geometry and the measured in plane lattice parameter. Figures 2(a) and 2(b) show high magnification ADF and ABF images corresponding to a MFTJ formed by a nine unit-cell PTO layer. The atomic number contrast from the ADF image shows a sharp and defect free interface. Using the atomic number contrast of ADF images, intensity profiles taken along the interface suggests that the termination is TiO_2 (From LSMO to PTO as shown in Fig. 2(c)). The ABF image shows the position of the oxygen columns (in addition to the cation positions), revealing the octahedral tilting in the LSMO, and the polar displacements in the PTO. Figure 2(d) shows a map of the out of plane displacements of the oxygen with respect to the A-sites, revealing both the polar displacements and tilting. The oxygen tilting is clearly visible in the LSMO as a chequerboard pattern, and the ferroelectric displacements reveal two 180° domain walls within the PTO. However, the transition between the two crystal structures is not immediately obvious.

To explore the polarisation and tilt at the interface, experimental profiles of both tilt and polar displacements going from LSMO into PTO are shown in Figure 3. The profiles have been split between the up, $P_\uparrow$, and down, $P_\downarrow$, polarisation domains. Within the PTO layer, the polar displacements are 23.7 ± 0.3 pm and -28.9 ± 0.8 pm (Fig. 3(a), corresponding to polarisations of 65 ± 1 μC cm^{-2} and -80 ± 2 μC cm^{-2} respectively, which are reduced from the bulk value of 84 μC cm^{-2}. This is possibly a result of asymmetric screening of the positive and negative charge (LSMO is a p-type conductor), but could also be related to structural distortions discussed later. The average octahedral tilt values in the LSMO (a few layers away from the interface with the PTO) are $5.45 \pm 0.09°$ and $5.24 \pm 0.07°$ for the up and down polarisation respectively. This values corresponds to a reduction in the MnO_6 octahedral tilt from the bulk value of 7.8°, as might be expected for a fully strained thin film.[27,29] The tilting in the PTO, and polarity in the LSMO is zero, as expected for from the bulk structures.

Interestingly, within one or two unit-cells of the LSMO-PTO interface, drastic differences in the polar displacements and tilt can be observed for the two domains. For the $P_\uparrow$ case, the polarisation at the interface is practically suppressed whilst there is some tilting (~3°). Conversely, the interface below a $P_\downarrow$ domain has bulk

like polarisation at the interface with complete suppression of the oxygen octahedral tilt. This behaviour at the interface agrees with the expected incompatibility of polar displacements and octahedral tilting. Previous studies have shown that it is possible for tilted structures to induce tilt in non-tilted structures due to cage connectivity.[44,45] However, the origin of the polarisation dependence in this system is not yet clear.

Unexpectedly, the $P_\downarrow$ domain with larger polar displacement has a smaller tetragonality within the layer (c/a ratio of 1.035 ± 0.002) compared to the $P_\uparrow$ domain (c/a ratio of 1.061 ± 0.004). This may be a result of strain caused by opposing movements of both the Ti and Pb atoms, and therefore the [100] atomic planes, across the domain wall in the PTO.[46,47] The asymmetry between the polarisation magnitude noted above may be a result of this strain effect. This is particularly evident at the interface, where the c lattice parameter is significantly larger for the polarisation down case. This may be an important component in allowing the tilting of the oxygen octahedra with polar displacement as the restrictions due to the atomic sizes are relaxed.

DFT calculations carried out on the LSMO/PTO system suggest that the charged layer structure of the LSMO is the main source of the differences in interface polarisation. In a similar fashion to the arguments made for LaAlO$_3$,[48] LSMO can be thought of as consisting of (La, Sr)O and MnO$_2$ (100) planes, each of non-zero charge (with (La, Sr)O +0.7 and MnO$_2$ -0.7, as shown in Fig. 4(a). These charged planes create an effective polarisation, or surface bound charge, of +/-0.35 e^- per 2D formula unit in the underlying ionic lattice (which is screened by its own free charges, being a metal). Depending on the interface termination, the LSMO effective polarisation will act to screen or reinforced the bound charges arising from the PTO layer at the interface, as shown schematically in Fig. 4. For example, the system presented here has an interfacial termination type TiO$_2$-(La, Sr)O, therefore the positive (La, Sr)O interface will screen/reinforce the negative/positive bound charge for the $P_\uparrow$/$P_\downarrow$ domains in the PTO.

Since LSMO is a poor metal (and therefore has a large screening length), an interface charge layer composed of free and bound charges is created. The system responds to this effect through local cation off-centring within this region. The competition between the tilt structure and polarisation is then driven by this polarisation screening and the structure is allowed to become more bulk-like when the total bound charge (coming from both LSMO and PTO polarisations) is lower. This is also reflected in the structural results of the DFT calculations shown in the supporting information.

This has implications for the design of some devices that are dependent on the magnetic properties of the interface. For example, ferroelectric field effect devices have been demonstrated that use ferroelectric layers to modulate the splitting of Mn orbitals in adjacent LSMO. This coupling is then used to modify and control the electronic and magnetic properties [35,49,50] For example, the DFT calculations for the structure shown here (but for the MnO$_2$-PbO interface) show that the proportion of the Mn $3d$ e_g orbitals consisting of z^2 is 54.6 % for $P_\downarrow$ vs 37.6 % for $P_\uparrow$ (occupation for in plane only polarisation is 45.4 %). This agrees with previous studies showing the structural distortions in LSMO provide such an effect. However, it is shown here that the structural changes depend on the interface termination, so therefore the preference of the z^2 and $x^2 - y^2$ orbitals also depends on the interface termination. This is a critical consideration when designing and fabricating any such device.

Furthermore, as the magnetic properties of LSMO depend on the O-Mn-O bonding (and therefore the Mn $3d$ and O $2p$ orbital overlap),[49] the reduction in octahedral tilting may be expected to increase the magnetisation of the interface.[44,51] However, DFT calculations indicate that this effect is quite small (3.562 μ_B vs 3.572 μ_B for 4.5° tilted and untilted structures) compared to the effect of the free charge accumulation (3.759 μ_B vs 3.076 μ_B for $P_\downarrow$ and $P_\uparrow$ at a MnO_2 interface). As LSMO is a half metal, when free charge pools at the interface to screen the bound charges there is also an accumulation of spins that alters the magnetisation.[52] This charge accumulation is shown for the (La, Sr)O termination in Fig. 4(a)-(c) and the MnO_2 termination in Fig. 4(e)-(g). The DFT calculated magnetisation profiles, shown in Figs. 4(d) and 4(h), correlate well with these free screening charge accumulation/depletion schematics. It is then evident that whereas the relation between the tilting and polarisation is dependent on the interface termination, the determining factor in modulating the magnetisation at the interface is the polarisation direction.

The difference between the TMR loops of the two polarisation directions, shown in Fig. 5, demonstrate this experimentally. It can be seen that the $P_\downarrow$ state, where the interface tilts are lower, has a higher TMR ratio (40 % for $P_\downarrow$ vs 33 % for $P_\uparrow$). This correlates with the higher interface magnetisation as a result of the free charge accumulation (as a result of the polarisation bound charge) but inversely correlates with the LSMO interface tilt. This again shows that the dominant effect is charge (and therefore spin) accumulation at the interface, which is polarisation dependent but comparatively interface independent.

Conclusions

It has been shown here that the simple picture of uniform symmetric screening of ferroelectric polarisation at the ferroelectric metal interfaces is not valid. A combination of atomic resolution TEM and DFT has been used to show how octahedral rotations and polarisation interact at the PTO-LSMO interface. Here, there is a competition between the structures of the two materials that is strongly dependent on the polarisation direction and the interface termination. This results in two different screening regimes (where the interface charge acts with or against the free charge) of the polarisation in the ferroelectric film depending on the polarisation direction. Controlling the termination, or even providing a completely different interface composition, provides a path to controlling and optimising ferroelectric and magnetic properties, particularly for ultrathin films where the interface effects are more pronounced. This is particularly relevant for the design of devices such as FEFEDs and MFTJs, as well as in ferroelectric multilayers, with several interfaces and often more complex polarisation.

Supporting Information

DFT structural calculations of polar displacement and octahedral tilt for the PTO-LSMO system with MnO_2 interface termination (polarisation up and down) and La,SrO termination (polarisation up only).

Notes

The authors declare no competing financial interest. The dataset for this publication may be obtained from http://wrap.warwick.ac.uk/130099.

References

(1)   Batra, I. P.; Wurfel, P.; Silverman, B. D. Phase Transition, Stability, and Depolarization Field in Ferroelectric Thin Films. *Phys. Rev. B* **1973**, *8* (7), 3257–3265. https://doi.org/10.1103/PhysRevB.8.3257.

(2)   Batra, I. P.; Silverman, B. D. Thermodynamic Stability of Thin Ferroelectric Films. *Solid State Communications* **1972**, *11* (1), 291–294. https://doi.org/10.1016/0038-1098(72)91180-5.

(3)   Kretschmer, R.; Binder, K. Surface Effects on Phase Transitions in Ferroelectrics and Dipolar Magnets. *Phys. Rev. B* **1979**, *20* (3), 1065–1076. https://doi.org/10.1103/PhysRevB.20.1065.

(4)   Tilley, D. R. Finite Size Effects on Phase Transitions in Ferroelectrics. In *Ferroelectric Thin Films: Synthesis and Basic Properties*; Gordon and Breach, 1996.

(5)   Fong, D. D.; Stephenson, G. B.; Streiffer, S. K.; Eastman, J. A.; Auciello, O.; Fuoss, P. H.; Thompson, C. Ferroelectricity in Ultrathin Perovskite Films. *Science* **2004**, *304* (5677), 1650–1653. https://doi.org/10.1126/science.1098252.

(6)   Peters, J. J. P.; Apachitei, G.; Beanland, R.; Alexe, M.; Sanchez, A. M. Polarization Curling and Flux Closures in Multiferroic Tunnel Junctions. *Nature Communications* **2016**, *7*, 13484. https://doi.org/10.1038/ncomms13484.

(7)   Tenne, D. A.; Turner, P.; Schmidt, J. D.; Biegalski, M.; Li, Y. L.; Chen, L. Q.; Soukiassian, A.; Trolier-McKinstry, S.; Schlom, D. G.; Xi, X. X.; et al. Ferroelectricity in Ultrathin BaTiO 3 Films: Probing the Size Effect by Ultraviolet Raman Spectroscopy. *Physical Review Letters* **2009**, *103* (17). https://doi.org/10.1103/PhysRevLett.103.177601.

(8)   Maksymovych, P.; Huijben, M.; Pan, M.; Jesse, S.; Balke, N.; Chu, Y.-H.; Chang, H. J.; Borisevich, A. Y.; Baddorf, A. P.; Rijnders, G.; et al. Ultrathin Limit and Dead-Layer Effects in Local Polarization Switching of $BiFeO_3$. *Phys. Rev. B* **2012**, *85* (1), 014119. https://doi.org/10.1103/PhysRevB.85.014119.

(9)   Yadav, A. K.; Nelson, C. T.; Hsu, S. L.; Hong, Z.; Clarkson, J. D.; Schlepüetz, C. M.; Damodaran, A. R.; Shafer, P.; Arenholz, E.; Dedon, L. R.; et al. Observation of Polar Vortices in Oxide Superlattices. *Nature* **2016**, *530* (7589), 198–201. https://doi.org/10.1038/nature16463.

(10)   Hwang, H. Y.; Iwasa, Y.; Kawasaki, M.; Keimer, B.; Nagaosa, N.; Tokura, Y. Emergent Phenomena at Oxide Interfaces. *Nature Materials* **2012**, *11*, 103–113.

(11)   Gerra, G.; Tagantsev, A. K.; Setter, N.; Parlinski, K. Ionic Polarizability of Conductive Metal Oxides and Critical Thickness for Ferroelectricity in $BaTiO_3$. *Physical Review Letters* **2006**, *96* (10). https://doi.org/10.1103/PhysRevLett.96.107603.

(12)   Prosandeev, S.; Bellaiche, L. Asymmetric Screening of the Depolarizing Field in a Ferroelectric Thin Film. *Phys. Rev. B* **2007**, *75* (17), 172109. https://doi.org/10.1103/PhysRevB.75.172109.

(13)   Yang, Q.; Cao, J. X.; Ma, Y.; Zhou, Y. C.; Lou, X. J.; Yang, J. Interface Effect on the Magnitude and Stability of Ferroelectric Polarization in Ultrathin $PbTiO_3$ Films from First-

Principles Study. *Journal of Applied Physics* **2013**, *114* (3), 034109. https://doi.org/10.1063/1.4816350.

(14) Ohtomo, A.; Hwang, H. Y. A High-Mobility Electron Gas at the LaAlO$_3$/SrTiO$_3$ Heterointerface. *Nature* **2004**, *427* (6973), 423–426. https://doi.org/10.1038/nature02308.

(15) Takahashi, K. S.; Kawasaki, M.; Tokura, Y. Interface Ferromagnetism in Oxide Superlattices of CaMnO$_3$/CaRuO$_3$. *Appl. Phys. Lett.* **2001**, *79* (9), 1324–1326. https://doi.org/10.1063/1.1398331.

(16) Wang, F.; Ren, Z.; Tian, H.; Yang, S. A.; Xie, Y.; Lu, Y.; Jiang, J.; Han, G.; Yang, K. Interfacial Multiferroics of TiO2/PbTiO3 Heterostructure Driven by Ferroelectric Polarization Discontinuity. *ACS Appl. Mater. Interfaces* **2017**, *9* (2), 1899–1906. https://doi.org/10.1021/acsami.6b13183.

(17) Lu, Y.; Wang, F.; Chen, M.; Lan, Z.; Ren, Z.; Tian, H.; Yang, K. Tuning Interfacial Magnetic Ordering via Polarization Control in Ferroelectric SrTiO3/PbTiO3 Heterostructure. *ACS Appl. Mater. Interfaces* **2018**, *10* (12), 10536–10542. https://doi.org/10.1021/acsami.7b19112.

(18) Quindeau, A.; Fina, I.; Marti, X.; Apachitei, G.; Ferrer, P.; Nicklin, C.; Pippel, E.; Hesse, D.; Alexe, M. Four-State Ferroelectric Spin-Valve. *Scientific Reports* **2015**, *5*, 9749. https://doi.org/10.1038/srep09749.

(19) Pantel, D.; Alexe, M. Electroresistance Effects in Ferroelectric Tunnel Barriers. *Phys. Rev. B* **2010**, *82* (13), 134105. https://doi.org/10.1103/PhysRevB.82.134105.

(20) Zhang, S.; Zhu, Y.; Tang, Y.; Liu, Y.; Li, S.; Han, M.; Ma, J.; Wu, B.; Chen, Z.; Saremi, S.; et al. Giant Polarization Sustainability in Ultrathin Ferroelectric Films Stabilized by Charge Transfer. *Advanced Materials* **2017**, *29* (46), 1703543. https://doi.org/10.1002/adma.201703543.

(21) Pantel, D.; Goetze, S.; Hesse, D.; Alexe, M. Reversible Electrical Switching of Spin Polarization in Multiferroic Tunnel Junctions. *Nat Mater* **2012**, *11* (4), 289–293. https://doi.org/10.1038/nmat3254.

(22) Quindeau, A.; Borisov, V.; Fina, I.; Ostanin, S.; Pippel, E.; Mertig, I.; Hesse, D.; Alexe, M. Origin of Tunnel Electroresistance Effect in PbTiO$_3$-Based Multiferroic Tunnel Junctions. *Phys. Rev. B* **2015**, *92* (3), 035130. https://doi.org/10.1103/PhysRevB.92.035130.

(23) Borisov, V. S.; Ostanin, S.; Achilles, S.; Henk, J.; Mertig, I. Spin-Dependent Transport in a Multiferroic Tunnel Junction: Theory for Co/PbTiO$_3$/Co. *Phys. Rev. B* **2015**, *92* (7), 075137. https://doi.org/10.1103/PhysRevB.92.075137.

(24) Boschker, H.; Verbeeck, J.; Egoavil, R.; Bals, S.; van Tendeloo, G.; Huijben, M.; Houwman, E. P.; Koster, G.; Blank, D. H. A.; Rijnders, G. Preventing the Reconstruction of the Polar Discontinuity at Oxide Heterointerfaces. *Adv. Funct. Mater.* **2012**, *22* (11), 2235–2240. https://doi.org/10.1002/adfm.201102763.

(25) Guo, E.-J.; Charlton, T.; Ambaye, H.; Desautels, R. D.; Lee, H. N.; Fitzsimmons, M. R. Orientation Control of Interfacial Magnetism at La$_{0.67}$Sr$_{0.33}$MnO$_3$/SrTiO$_3$ Interfaces. *ACS Appl. Mater. Interfaces* **2017**, *9* (22), 19307–19312. https://doi.org/10.1021/acsami.7b03252.

(26) Glazer, A. M. The Classification of Tilted Octahedra in Perovskites. *Acta Crystallographica Section B: Structural Crystallography and Crystal Chemistry* **1972**, *28* (11), 3384–3392.

(27) He, J.; Borisevich, A.; Kalinin, S. V.; Pennycook, S. J.; Pantelides, S. T. Control of Octahedral Tilts and Magnetic Properties of Perovskite Oxide Heterostructures by Substrate Symmetry. *Physical Review Letters* **2010**, *105* (22). https://doi.org/10.1103/PhysRevLett.105.227203.

(28) Borisevich, A. Y.; Chang, H. J.; Huijben, M.; Oxley, M. P.; Okamoto, S.; Niranjan, M. K.; Burton, J. D.; Tsymbal, E. Y.; Chu, Y. H.; Yu, P.; et al. Suppression of Octahedral Tilts and Associated Changes in Electronic Properties at Epitaxial Oxide Heterostructure Interfaces. *Phys. Rev. Lett.* **2010**, *105* (8), 087204. https://doi.org/10.1103/PhysRevLett.105.087204.

(29) Gao, Y.; Wang, J.; Wu, L.; Bao, S.; Shen, Y.; Lin, Y.; Nan, C. Tunable Magnetic and Electrical Behaviors in Perovskite Oxides by Oxygen Octahedral Tilting. *Science China Materials* **2015**, *58* (4), 302–312. https://doi.org/10.1007/s40843-015-0047-0.

(30) Kim, Y.-M.; Kumar, A.; Hatt, A.; Morozovska, A. N.; Tselev, A.; Biegalski, M. D.; Ivanov, I.; Eliseev, E. A.; Pennycook, S. J.; Rondinelli, J. M.; et al. Interplay of Octahedral Tilts and Polar Order in $BiFeO_3$ Films. *Adv. Mater.* **2013**, *25* (17), 2497–2504. https://doi.org/10.1002/adma.201204584.

(31) Benedek, N. A.; Fennie, C. J. Why Are There So Few Perovskite Ferroelectrics? *J. Phys. Chem. C* **2013**, *117* (26), 13339–13349. https://doi.org/10.1021/jp402046t.

(32) Burton, J. D.; Tsymbal, E. Y. Prediction of Electrically Induced Magnetic Reconstruction at the Manganite/Ferroelectric Interface. *Phys. Rev. B* **2009**, *80* (17), 174406. https://doi.org/10.1103/PhysRevB.80.174406.

(33) Bristowe, N. C.; Stengel, M.; Littlewood, P. B.; Pruneda, J. M.; Artacho, E. Electrochemical Ferroelectric Switching: Origin of Polarization Reversal in Ultrathin Films. *Phys. Rev. B* **2012**, *85* (2), 024106. https://doi.org/10.1103/PhysRevB.85.024106.

(34) Hammouri, M.; Fohtung, E.; Vasiliev, I. Ab Initio Study of Magnetoelectric Coupling in $La_{0.66}Sr_{0.33}MnO_3$ / $PbZr_{0.2}Ti_{0.8}O_3$ Multiferroic Heterostructures. *J. Phys.: Condens. Matter* **2016**, *28* (39), 396004. https://doi.org/10.1088/0953-8984/28/39/396004.

(35) Preziosi, D.; Alexe, M.; Hesse, D.; Salluzzo, M. Electric-Field Control of the Orbital Occupancy and Magnetic Moment of a Transition-Metal Oxide. *Physical Review Letters* **2015**, *115* (15). https://doi.org/10.1103/PhysRevLett.115.157401.

(36) Yu, X.; Wu, L.; Zhang, B.; Zhou, H.; Dong, Y.; Wu, X.; Kou, R.; Yang, P.; Chen, J.; Sun, C.-J.; et al. Thickness-Dependent Polarization-Induced Intrinsic Magnetoelectric Effects in $La_{0.67}Sr_{0.33}MnO_3/PbZr_{0.52}Ti_{0.48}O_3$ Heterostructures. *Phys. Rev. B* **2019**, *100* (10), 104405. https://doi.org/10.1103/PhysRevB.100.104405.

(37) Findlay, S. D.; Shibata, N.; Sawada, H.; Okunishi, E.; Kondo, Y.; Ikuhara, Y. Dynamics of Annular Bright Field Imaging in Scanning Transmission Electron Microscopy. *Ultramicroscopy* **2010**, *110* (7), 903–923. https://doi.org/10.1016/j.ultramic.2010.04.004.

(38) Wu, Z.; Cohen, R. E. More Accurate Generalized Gradient Approximation for Solids. *Phys. Rev. B* **2006**, *73* (23), 235116. https://doi.org/10.1103/PhysRevB.73.235116.

(39) Ordejón, P.; Artacho, E.; Soler, J. M. Self-Consistent Order-N Density-Functional Calculations for Very Large Systems. *Phys. Rev. B* **1996**, *53* (16), R10441–R10444. https://doi.org/10.1103/PhysRevB.53.R10441.

(40) Soler, J. M.; Artacho, E.; Gale, J. D.; García, A.; Junquera, J.; Ordejón, P.; Sánchez-Portal, D. The SIESTA Method for Ab Initio Order-N Materials Simulation. *J. Phys.: Condens. Matter* **2002**, *14* (11), 2745. https://doi.org/10.1088/0953-8984/14/11/302.

(41) Ferrari, V.; Pruneda, J. M.; Artacho, E. Density Functionals and Half-Metallicity in La2/3Sr1/3MnO3. *physica status solidi (a)* **2006**, *203* (6), 1437–1441. https://doi.org/10.1002/pssa.200566183.

(42) Junquera, J.; Zimmer, M.; Ordejón, P.; Ghosez, P. First-Principles Calculation of the Band Offset at $BaO/BaTiO_3$ and $SrO/SrTiO_3$ Interfaces. *Phys. Rev. B* **2003**, *67* (15), 155327. https://doi.org/10.1103/PhysRevB.67.155327.

(43) Stengel, M.; Aguado-Puente, P.; Spaldin, N. A.; Junquera, J. Band Alignment at Metal/Ferroelectric Interfaces: Insights and Artifacts from First Principles. *Phys. Rev. B* **2011**, *83* (23), 235112. https://doi.org/10.1103/PhysRevB.83.235112.

(44) Sanchez-Santolino, G.; Cabero, M.; Varela, M.; Garcia-Barriocanal, J.; Leon, C.; Pennycook, S. J.; Santamaria, J. Oxygen Octahedral Distortions in $LaMO_3/SrTiO_3$ Superlattices. *Microscopy and Microanalysis* **2014**, *20* (03), 825–831. https://doi.org/10.1017/S1431927614000750.

(45) Aso, R.; Kan, D.; Shimakawa, Y.; Kurata, H. Octahedral Tilt Propagation Controlled by A-Site Cation Size at Perovskite Oxide Heterointerfaces. *Crystal Growth & Design* **2014**, *14* (5), 2128–2132. https://doi.org/10.1021/cg500285m.

(46) Aguado-Puente, P.; Junquera, J. Structural and Energetic Properties of Domains in PbTiO$_3$/SrTiO$_3$ Superlattices from First Principles. *Physical Review B* **2012**, *85* (18). https://doi.org/10.1103/PhysRevB.85.184105.

(47) Meyer, B.; Vanderbilt, D. *Ab Initio* Study of Ferroelectric Domain Walls in PbTiO$_3$. *Physical Review B* **2002**, *65* (10). https://doi.org/10.1103/PhysRevB.65.104111.

(48) Bristowe, N. C.; Littlewood, P. B.; Artacho, E. The Net Charge at Interfaces between Insulators. *J. Phys.: Condens. Matter* **2011**, *23* (8), 081001. https://doi.org/10.1088/0953-8984/23/8/081001.

(49) Tokura, Y. Orbital Physics in Transition-Metal Oxides. *Science* **2000**, *288* (5465), 462–468. https://doi.org/10.1126/science.288.5465.462.

(50) Chen, H.; Qiao, Q.; Marshall, M. S. J.; Georgescu, A. B.; Gulec, A.; Phillips, P. J.; Klie, R. F.; Walker, F. J.; Ahn, C. H.; Ismail-Beigi, S. Reversible Modulation of Orbital Occupations via an Interface-Induced Polar State in Metallic Manganites. *Nano Lett.* **2014**, *14* (9), 4965–4970. https://doi.org/10.1021/nl501209p.

(51) Li, Z.; Song, D.; Yu, R.; Ge, B.; Liao, Z.; Li, Y.; Dong, S.; Zhu, J. Competing Interfacial Reconstruction Mechanisms in La$_{0.7}$Sr$_{0.3}$MnO$_3$/SrTiO$_3$ Heterostructures. *ACS Applied Materials & Interfaces* **2016**, *8* (36), 24192–24197. https://doi.org/10.1021/acsami.6b07569.

(52) Spurgeon, S. R.; Balachandran, P. V.; Kepaptsoglou, D. M.; Damodaran, A. R.; Karthik, J.; Nejati, S.; Jones, L.; Ambaye, H.; Lauter, V.; Ramasse, Q. M.; et al. Polarization Screening-Induced Magnetic Phase Gradients at Complex Oxide Interfaces. *Nat Commun* **2015**, *6*, 6735. https://doi.org/10.1038/ncomms7735.
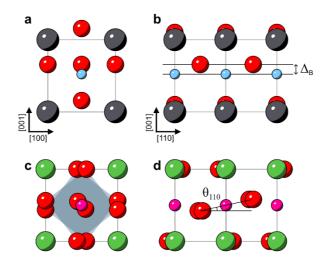
Figure 1 Ferroelectric PTO structure as viewed along the 100, (a), and 110, (b). LSMO structure view along the 100, (c), and 110, (d). The measured ferroelectric displacements Δ_B and the octahedral tilt angle, θ_{110}, have been labelled.
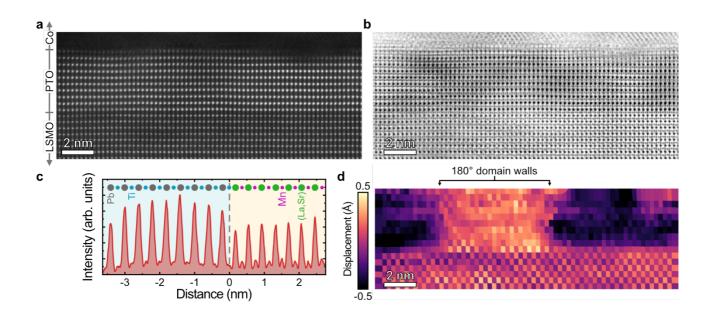
Figure 2 (a) ADF and (b) ABF images of the LSMO-PTO-Co FTJ. Contrast in the ADF image gives elemental information, with higher atomic number elements being brighter. (c) out of plane ADF intensity profile where the atomic columns have been identified. (d) map of the out of plane displacements of the O columns with respect to the A lattice.
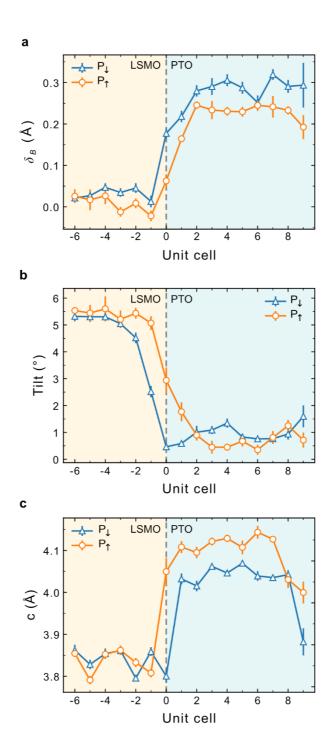
Figure 3 (a) Experimental out of plane displacement, (b) octahedral tilting and (c) c lattice parameters as a function of unit cell from LSMO to the PTO-Co interface. Profiles for both the up and down domains are shown. The displacement for the polarisation down case has been inverted for comparison with the polarisation up case. Values are in plane averaged within each domain, error bars are the standard errors of the means.
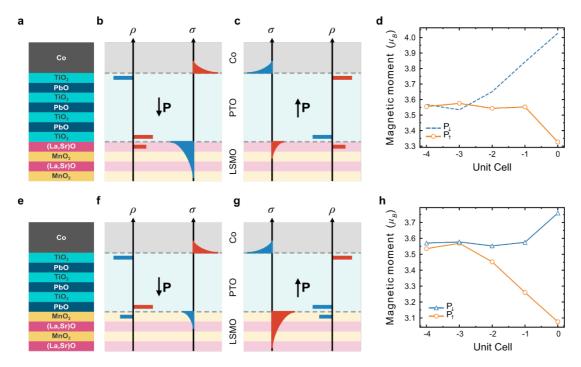
Figure 4 (a) Schematic of the layered structure in the FTJ device with (La,Sr)O termination. Corresponding schematic of bound charge, ρ, and the screening charges, σ, for polarisation directions down, (b), and up, (c). Negative charge shown in blue, positive in red. (d) Corresponding DFT calculations of the Mn magnetic moment as a function of unit cell from the interface for the two polarisation directions. The 0th unit cell is closest to PTO. (e)-(h) show the same as (a)-(d) but for the MnO_2 terminated interface. Due to the DFT limitations (see Methods section for details), (d) shows an estimate for the $P_\downarrow$ magnetic moments (dashed line) as the inverted $P_\uparrow$ profile from (h).
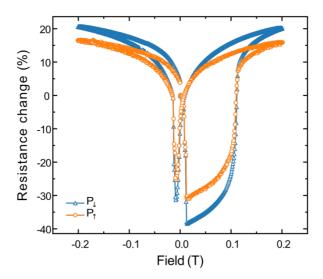
Figure 5 Experimental TMR loops for the two polarisation directions. Resistance changes are given as a percentage of the as-grown ground state.

Table of contents graphic